Original Article

Healthc Inform Res. 2016 October;22(4):316-325.
https://doi.org/10.4258/hir.2016.22.4.316
pISSN 2093-3681 • eISSN 2093-369X

HIR
Healthcare Informatics Research

Half-Fan-Based Intensity-Weighted Region-of-Interest Imaging for Low-Dose Cone-Beam CT in Image-Guided Radiation Therapy

Boyeol Yoo, MS[1], Kihong Son, MS[1], Rizza Pua, PhD[1], Jinsung Kim, PhD[2], Alexander Solodov, PhD[3], Seungryong Cho, PhD[1]

[1]Department of Nuclear and Quantum Engineering, Korea Advanced Institute of Science and Technology, Daejeon, Korea; [2]Department of Radiation Oncology, Yonsei Cancer Center, Yonsei University College of Medicine, Seoul, Korea; [3]Department of Nuclear Engineering, Khalifa University, Abu Dhabi, UAE

Objectives: With the increased use of computed tomography (CT) in clinics, dose reduction is the most important feature people seek when considering new CT techniques or applications. We developed an intensity-weighted region-of-interest (IWROI) imaging method in an exact half-fan geometry to reduce the imaging radiation dose to patients in cone-beam CT (CBCT) for image-guided radiation therapy (IGRT). While dose reduction is highly desirable, preserving the high-quality images of the ROI is also important for target localization in IGRT. **Methods:** An intensity-weighting (IW) filter made of copper was mounted in place of a bowtie filter on the X-ray tube unit of an on-board imager (OBI) system such that the filter can substantially reduce radiation exposure to the outer ROI. In addition to mounting the IW filter, the lead-blade collimation of the OBI was adjusted to produce an exact half-fan scanning geometry for a further reduction of the radiation dose. The chord-based rebinned backprojection-filtration (BPF) algorithm in circular CBCT was implemented for image reconstruction, and a humanoid pelvis phantom was used for the IWROI imaging experiment. **Results:** The IWROI image of the phantom was successfully reconstructed after beam-quality correction, and it was registered to the reference image within an acceptable level of tolerance. Dosimetric measurements revealed that the dose is reduced by approximately 61% in the inner ROI and by 73% in the outer ROI compared to the conventional bowtie filter-based half-fan scan. **Conclusions:** The IWROI method substantially reduces the imaging radiation dose and provides reconstructed images with an acceptable level of quality for patient setup and target localization. The proposed half-fan-based IWROI imaging technique can add a valuable option to CBCT in IGRT applications.

Keywords: Cone-Beam Computed Tomography, Low-Dose, Region-of-Interest, Half-Fan, Image-Guided Radiation Therapy

Submitted: September 18, 2016
Revised: September 29, 2016
Accepted: September 30, 2016

Corresponding Author
Seungryong Cho, PhD
Department of Nuclear and Quantum Engineering, Korea Advanced Institute of Science and Technology (KAIST), 291 Daehak-ro, Yuseong-gu, Daejeon 34141, Korea. Tel: +82-42-350-3828, E-mail: scho@kaist.ac.kr

I. Introduction

Image-guided radiation therapy (IGRT) increases therapeutic efficiency by confirming the patient position and target location prior to delivering therapeutic radiation [1]. Cone-beam computed tomography (CBCT) is one of the most widely used imaging modalities in IGRT, as it provides rich anatomic information, is relatively easy to manipulate, and can be directly associated with the planning CT images. CBCT images are registered to the diagnostic CT image that was used for the treatment planning, with the patient and target positions accordingly aligned. In spite of its usefulness in IGRT, CBCT must be carefully managed in terms of the radiation dose, particularly in repeated scans or daily CBCT applications [2]. Much effort has been directed toward reducing the radiation dose in CBCT. Examples include sparse-view sampling and low-tube-current scanning methods. Iterative algorithms for image reconstruction in conjunction with such sparse-view techniques have also been developed [3-8]. Although iterative algorithms are promising in such approaches, a low-dose technique based on analytical reconstruction has advantages over iterative reconstruction, such as fast computation and no requirement of case-dependent tunable parameters. In this study, we propose a half-fan-based intensity-weighted region-of-interest (IWROI) imaging technique for low-dose CBCT with an analytic reconstruction algorithm.

For the purpose of image guidance, one often needs a high-quality image of the ROI including the target while also requiring an image of the outside ROI, not necessarily of a high quality though, for image registration. Filter-based ROI imaging techniques have also been studied in a full-fan CBCT [9-11]. Similar ROI imaging ideas can be found in cone-beam rotational angiography and in C-arm CBCT [12,13]. In these applications, filters were placed in front of the X-ray tube such that they create regions of two different beam intensities: inner and outer ROIs. By sacrificing the image quality of the outer ROI region, it becomes possible reduce the overall imaging radiation dose to the patient. However, the clinical utility of this method is limited to a small field-of-view (FOV) owing to the reliance on a full-fan geometry. Although some truncation problems can be effectively handled in a full-fan geometry with the use of the chord-based backprojection-filtration (BPF) algorithm for image reconstruction [14,15] or with correction methods [16,17], in general they are challenging, particularly for obese patients. Indeed, a half-fan geometry is used for most treatment sites, including the chest and the abdomen, due to its enlarged FOV in CBCT. Therefore, in this work we propose a half-fan-based IWROI imaging technique for low-dose CBCT. It was observed that most CBCT systems that support half-fan scanning geometries place the detector such that the projection of the rotation axis is positioned with a substantial margin from the near-edge region of the detecting area. For example, the OBI system (Varian Medical Systems, Palo Alto, CA, USA) allocates a margin of 5 cm to the projection of the rotation axis due to the fact that reconstruction algorithms are mostly the filtered-backprojection (FBP) type in such systems and because the FBP algorithm requires additional off-axis data to avoid data discontinuity artifacts [16,18-20]. In contrast, the chord-based BPF algorithm does not require this type of extra data for image reconstruction because the filtering occurs after the backprojection onto the chords [21]. In an attempt to reduce the radiation dose further, we used an exact half-fan scanning geometry in which the off-axis margin is blocked by the collimator blade installed in the OBI source unit.

Li et al. [22] applied a BPF method for a cone-beam case of an asymmetric half-size detector. However, the BPF algorithm involves backprojection with a spatially varying weighting factor, which is computationally less efficient and numerically less stable. Yu et al. [23] developed a rebinned BPF algorithm for helical CBCT which does not have a spatially weighting factor in the formulation, demonstrating that the rebinned BPF algorithm produces higher image quality levels in terms of the noise level and its uniformity as compared to the ordinary BPF algorithm. In this study, the rebinned BPF algorithm was modified and implemented for use with half-fan data in a circular CBCT. Figure 1 shows a schematic of the scanning geometry used in this work.

This paper is organized as follows. We explain briefly the rebinning process from cone-beam to fan-parallel-beam data and the BPF algorithm utilizing the rebinned data in Section II. The system, filter, and phantoms used in the experiment and the method of heterogeneous beam-quality correction are described below. The results of the experiment, including the findings pertaining to the image quality, image registration, and dosimetric measurements, are reported in Section III. Finally, we discuss clinical implications of the proposed method.

II. Methods

Yu et al. [23] developed a rebinned BPF algorithm for image reconstruction in helical CBCT. We derive a modified algorithm for use in a half-fan circular CBCT in this work.

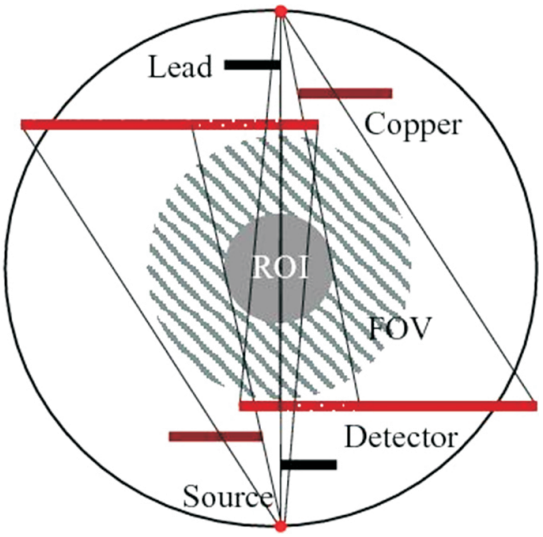

Figure 1. Intensity-weighted region-of-interest (IWROI) imaging schematic in a conventional half-fan geometry. FOV: field-of-view.

1. Image Reconstruction Algorithms

1) Rebinning from cone-beam to fan-parallel-beam data

Rebinned data can be expressed as $Q(\xi, v, \varphi)$ in the rebinned geometry coordinates (ξ, v, φ) that can be related to the cone-beam geometry coordinates (u, v, λ) [24], as follows,

$$Q(\xi, v, \varphi) = P(u, v, \lambda), \tag{1}$$

provided that

$$\xi = \frac{Ru}{\sqrt{u^2+S^2}} \text{ and } \varphi = \lambda - \arctan\frac{u}{S}, \tag{2}$$

where R and S represent the source-to-axis distance and the source-to-detector distance, respectively. A source position is represented by the angle λ, and u and v represent the flat-panel detector coordinates along the transverse and longitudinal directions, respectively. A schematic illustration after the rebinning of the data is shown in Figure 2.

2) BPF algorithm for circular CBCT

Because the reconstruction formula of the chord-based BPF algorithm has been explained in detail elsewhere [14,21], we summarize only briefly the essential steps in the BPF algorithm. A chord can be specified by λ_1 and λ_2 on a given source trajectory $\vec{r}_0(\lambda)$ parameterized by the angular variable λ. From cone-beam data $P(u, v, \lambda)$, one can compute a backprojection of the data derivatives onto the chord as

$$g_\pi(x'_\pi, \lambda_1, \lambda_2) = \int_{\lambda_1}^{\lambda_2} \frac{d\lambda}{\|\vec{r}-\vec{r}_0(\lambda)\|} \left[\frac{\partial}{\partial\lambda} \mathrm{P(u,v,\lambda)}\right]_{\hat{\beta}}, \tag{3}$$

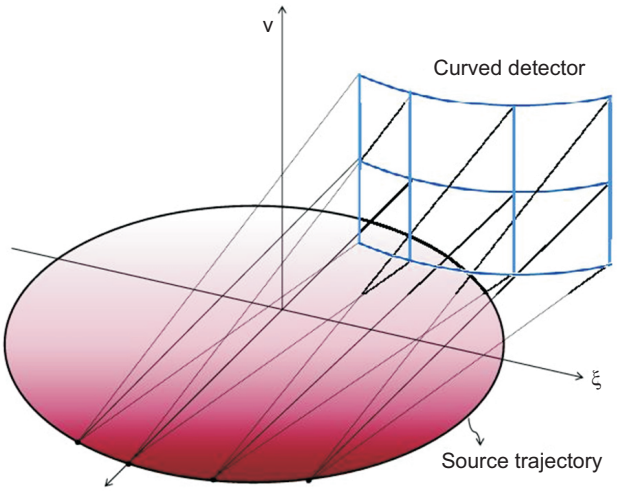

Figure 2. Schematic of a rebinned half-fan geometry.

where $\hat{\beta}$ denotes the direction of the ray from the source to the point of interest on the chord, and x_π indicates a point on the chord.

Based upon the backprojection g_π on the chord, the object function $f_\pi(x_\pi, \lambda_1, \lambda_2)$ on the chord is reconstructed by

$$f_\pi(x_\pi, \lambda_1, \lambda_2) = \frac{1}{2\pi^2} \frac{1}{\sqrt{(x_{\pi 1}-x_\pi)(x_\pi-x_{\pi 2})}} \times \int_{x_{\pi 1}}^{x_{\pi 2}} \frac{dx'_\pi}{x_\pi - x'_\pi} \sqrt{(x_{\pi 1}-x'_\pi)(x'_\pi - x_{\pi 2})} \times g_\pi(x'_\pi, \lambda_1, \lambda_2) + 2\pi P_0, \tag{4}$$

where $x_\pi \in [x_{\pi 1}, x_{\pi 2}]$ and where $x_{\pi 1}$ and $x_{\pi 2}$ define the object support on the chord. P_0 is the projection along the ray coinciding with the chord segment.

3) Rebinned BPF algorithm for the half-fan mode in circular CBCT

Equation (3) can be rewritten using Equations (1) and (2), as

$$g_\pi(x'_\pi, \lambda_1, \lambda_2) = \int_{\varphi_0}^{\varphi_{0+\pi}} \frac{d\varphi}{\|\vec{r}-\vec{r}_0(\lambda)\|} \left.\frac{d\lambda}{d\varphi}\right|_{\vec{r}'} \left[\frac{\partial}{\partial\lambda} \mathrm{Q}(\xi, v, \varphi)\right]_{\hat{\beta}}, \tag{5}$$

where φ_0 is one of the source positions that define a chord. Using the chain rule and the fact that v is not dependent on λ in a fan-parallel geometry in circular CBCT, one can obtain

$$\left.\frac{d}{d\lambda} Q(u, v, \varphi)\right|_{\hat{\beta}} = \sqrt{R^2 - \xi^2} \frac{\partial \mathrm{Q}(\xi, v, \varphi)}{\partial \xi}. \tag{6}$$

Computing $\frac{d\lambda}{d\varphi}$ from

 https://doi.org/10.4258/hir.2016.22.4.316

$$\left.\frac{d\lambda}{d\varphi}\right|_{\vec{r}'} = 1 - \frac{d}{du}\left(\arctan\frac{u}{S}\right)\cdot\left.\frac{du}{d\lambda}\right|_{\vec{r}'}$$

$$= 1 - \left(\frac{S^2-u^2}{S} - \frac{SR}{R-\vec{r}'\cdot\hat{e}_w(\lambda)}\right)\frac{S}{S^2+u^2}$$

$$= \frac{R^2-\xi^2}{RS}\,\frac{S}{\|\vec{r}'-\vec{r}_0(\lambda)\|}, \quad (7)$$

where $A = \sqrt{u2 + v2 + S2}$ and the relationship

$$\frac{A}{\|\vec{r}'-\vec{r}_0(\lambda)\|} = \frac{S}{R-\vec{r}'\cdot\hat{e}_w(\lambda)} \quad (8)$$

is used to obtain the last step of Equation (7), one can finally derive a rebinned BPF reconstruction formula for half-fan circular CBCT.

$$g_\pi(x'_\pi,\lambda_1,\lambda_2) = \int_{\varphi_0}^{\varphi_{0+\pi}} \frac{d\varphi}{\sqrt{1+(\frac{v}{S})^2(1-\frac{\xi^2}{R^2})}}\,\frac{\partial Q(\xi,v,\varphi)}{\partial\xi} - \int_{\varphi_{0+\pi}}^{\varphi_{0+2\pi}} \frac{d\varphi}{\sqrt{1+(-)^2(1-\frac{\xi^2}{R^2})}}\,\frac{\partial Q(\xi,v,\varphi)}{\partial\xi} \quad (9)$$

Clearly, the weighting factor $\sqrt{1+(\frac{v}{S})^2(1-\frac{\xi^2}{R^2})}$ becomes spatially invariant because it only depends on the detector coordinates ξ and v.

2. Experimental System and Scanning Configuration

We acquired data from the OBI system of Trilogy Tx (Varian Medical Systems). The OBI system has two robotic arms to carry a kilo-voltage X-ray source and a flat panel detector positioned orthogonally to the mega-voltage X-ray source for treatment.

Table 1. Scanning parameters used in the experiment

Parameter	Value
Source-to-axis distance	100 cm
Source-to-detector distance	150 cm
Number of views	Approximately 680
Detector array size	1,024 × 768
Pixel pitch	388 μm
Mode	Half-fan full-scan
kVp	125 kV
mA	80 mA
ms	13 ms

The scanning parameters used in this experiment are summarized in Table 1. It is important to note that we blocked 0.5 cm using a lead blade on the opposite side of copper filter to remove off-axis marginal data from the projections, as discussed in Section I. The dimensions of the intensity-weighting (IW) copper filter are 10 cm × 5.5 cm × 0.6 cm, and it was utilized instead of a half-fan bowtie filter. We selected 6 mm as an appropriate thickness of a copper filter that can achieve substantially reduced radiation exposure (approximately 90%) based on previous work by Cho et al. [11]. A dose reduction assessment is described in Section II-3.

3. Phantoms

A humanoid phantom (Rando, Alderson Associates, NY, USA) was used for the experiment (Figure 3). The pelvis part of the phantom was scanned. The phantom's soft tissue is made of a proprietary urethane formulation with an effective atomic number. The same phantom was also used for dose measurements with XRCT films and glass dosimeters inserted between the phantom slabs near the midplane of the scanning trajectory.

4. Heterogeneous Beam-Quality Correction

We calculated the log-transformed projection data (see Figure 4A) by taking the natural logarithm of the ratio of the open-field intensity map (see Figure 5A) to the raw projection of the phantom (see Figure 5B). The open-field intensity projection data were taken with identical scanning parameters and with the filter mounted but without the pelvis phantom. The dark region on the right side of the open-field image is due to filtering by the copper filter. It is necessary to use open-field data with the filter so that it can normalize the reduced beam intensity of the filtered area. However, the attenuation values of a scanned object in the filtered area are subject to beam-hardening through the filter, and they are underestimated compared to the unfiltered area. We noted that the shift of the mean energy of the X-rays was substantial; the mean energy of the X-ray spectrum at a tube voltage of 125 kV changes from 52.6 keV to 98.6 keV after being filtered by a 6-mm-thick copper filter.

A simple weighting method was applied to correct for this underestimation of the attenuation coefficients in the filtered region. The ratio of attenuation coefficients without and with the filter was obtained by dividing the projection data of a stack of solid water phantoms without the IW filter by that with the IW filter. A single anterior-posterior projection data without the IW filter was taken to calculate the ratio

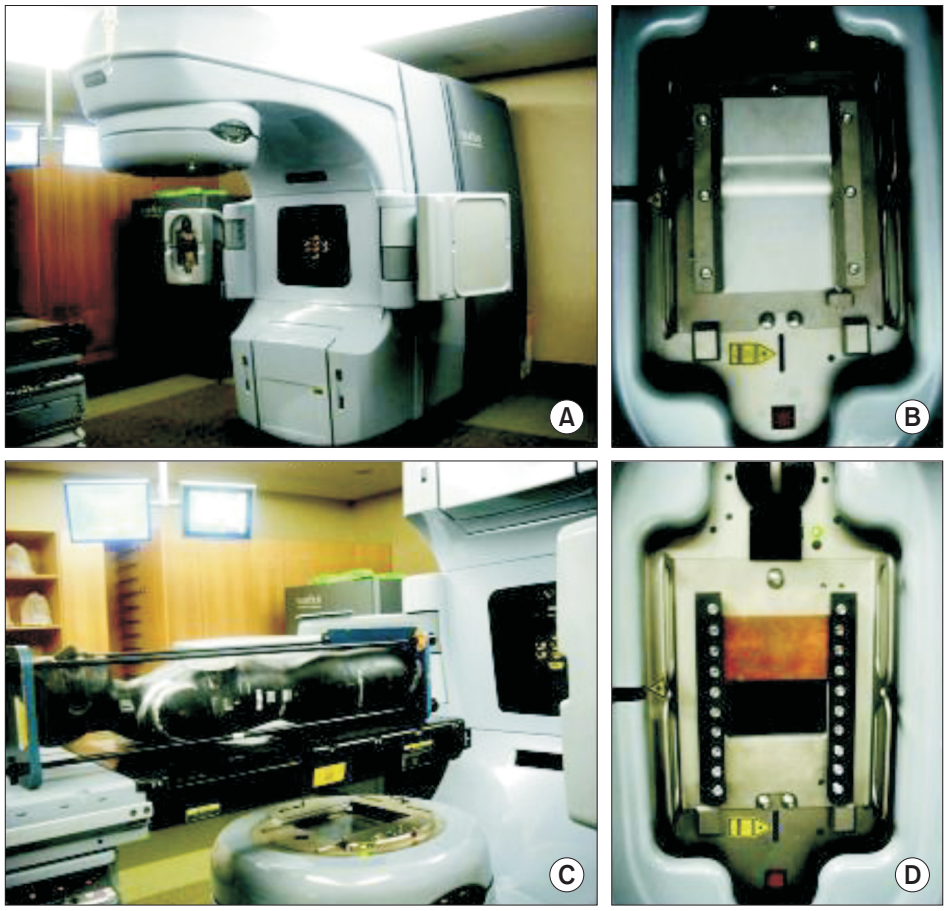

Figure 3. Images of (A) an on-board imager (OBI) system, (B) a mounted half-fan bowtie filter, (C) a humanoid phantom, and (D) a mounted intensity-weighting filter.

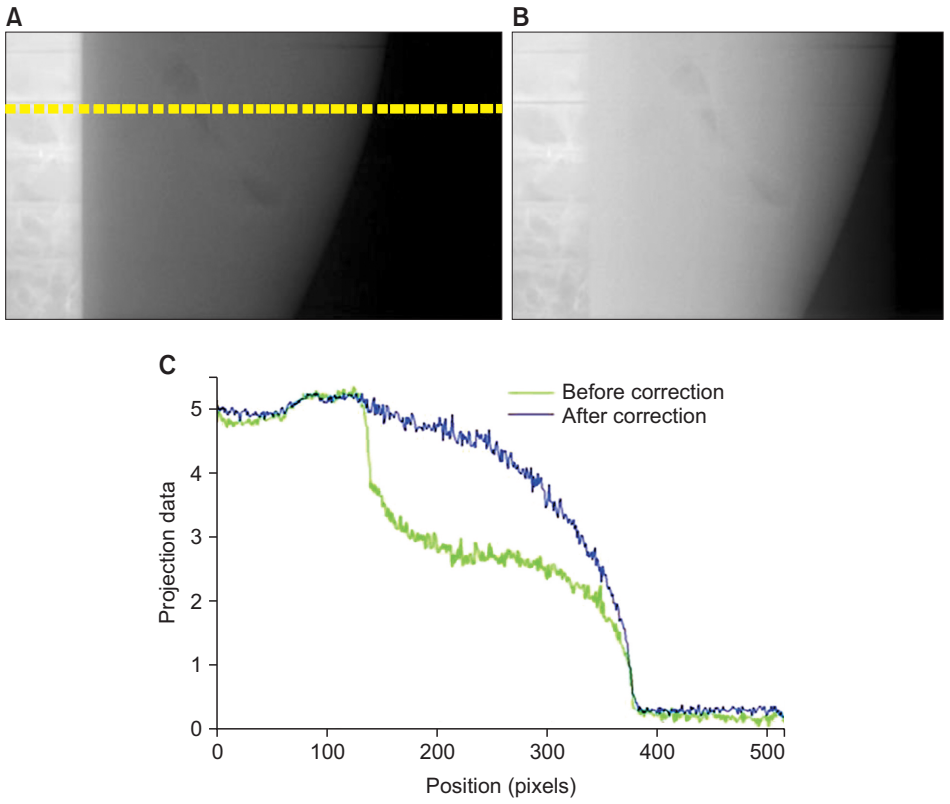

Figure 4. Log-transformed projection data (A) before and (B) after beam-quality correction. (C) Line profiles are shown for comparison. Note that the off-axis data are not shown.

https://doi.org/10.4258/hir.2016.22.4.316

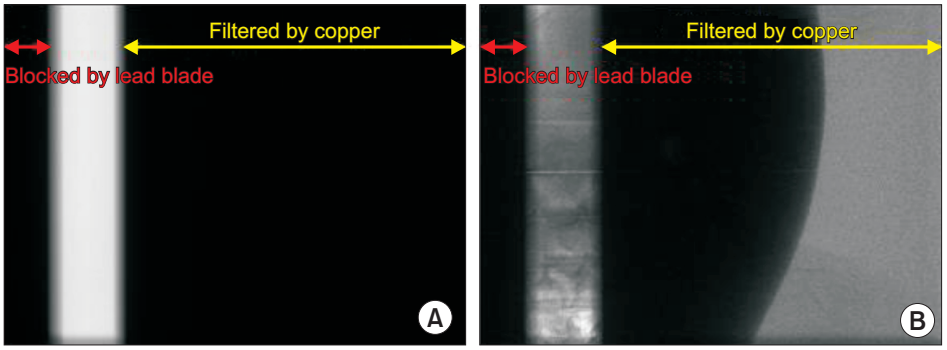

Figure 5. (A) An open-field intensity map and (B) a raw projection of a phantom.

map, and the acquired ratio map was multiplied to each log-transformed projection data. As shown in Figure 4B, the corrected data is nearly free from the heterogeneous beam-quality effects.

5. Image Registration

In order to validate the clinical utility of the IWROI images for IGRT, we performed an image registration task. We acquired a target image of the phantom using the OBI without a filter and used the IWROI image of the phantom as a moving image to be registered. A target image is supposed to preserve the fine quality of the bony structures in all regions of the image, while a moving image may lose a considerable amount of image information, particularly in the outer ROI region. We used the mutual-information-based rigid registration algorithm built into the visualization software Amira (Visage Imaging, San Diego, CA, USA).

6. Dosimetric Measurement

To assess the amount of dose reduction that is achieved by the proposed method, we used XRCT films and glass dosimeters calibrated for diagnostic X-ray energies. The film was placed in the Rando phantom near the midplane of the scanning trajectory. The film and glass dosimeters were placed such that it was possible to measure the radiation dose distribution from the inner ROI to the outer ROI (Figure 6). The scanning parameters listed in Table 1 were used in this case as well. Two consecutive OBI scans were conducted in each experiment to deliver enough radiation for the dose measurement. For comparison, we conducted three experiments: scanning without a filter, scanning with a half-fan bowtie filter, and scanning with the IW filter. As described earlier, a collimating blade was additionally utilized to block the off-axis margin in the scan with the IW filter. Film dose calibration was done using the software RIT113, V4 (Radiological Imaging Technology, Colorado Springs, CO, USA).

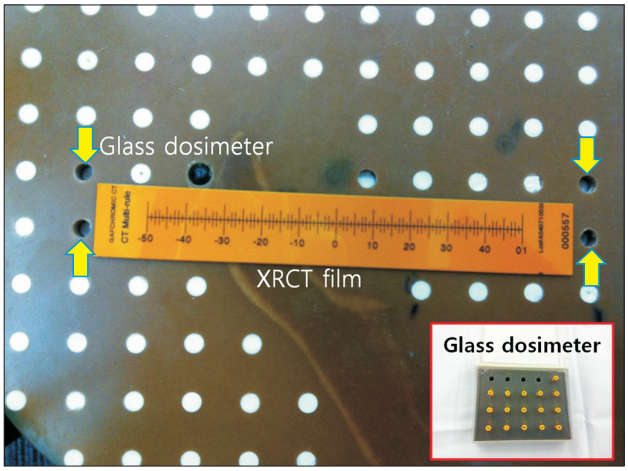

Figure 6. Film and glass dosimeters placed in the phantom for dosimetric measurements. XRCT: X-ray computed tomography.

III. Results

1. Image Reconstruction

The images were reconstructed by the rebinned BPF algorithm from the acquired data according to the proposed scanning method. We display reconstructed slice images of the pelvis phantom in Figure 7. The left column corresponds to the images reconstructed without heterogeneous beam-quality correction and the right column corresponds to those with beam-quality correction. The thick white ring artifact shown in Figure 7A is due to beam-quality heterogeneity, which is successfully removed after beam-quality correction, as shown in Figure 7B. The line profiles of the two images along the dashed line in the transverse slice, as depicted in Figure 7A, are shown in Figure 8. It is clearly shown that the heterogeneous beam quality causes strong peaks near the border of the inner and outer ROIs. Additionally, the reconstructed pixel values of the inner and outer ROIs are quite different in the images reconstructed without beam-quality correction.

Noise is directly related to the radiation dose. As is visually

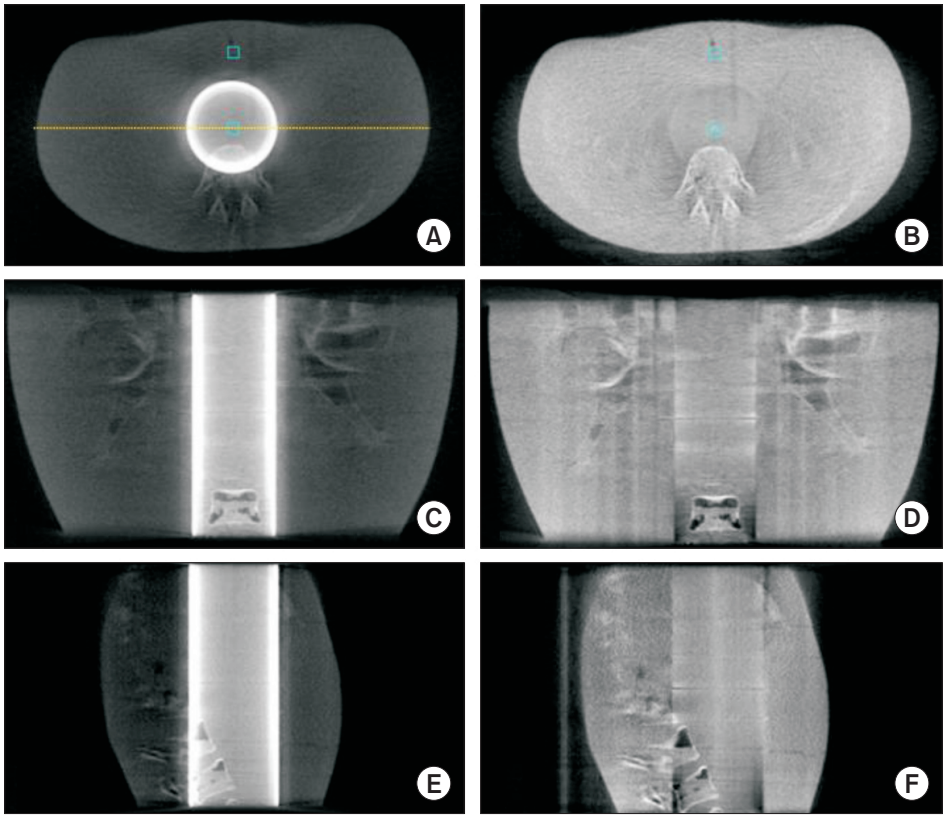

Figure 7. Transverse images (A) before and (B) after; coronal images (C) before and (D) after; and sagittal images (E) before and (F) after beam-quality correction. The display window is [10, 250] HU for the images on the left and [10, 160] HU for the images on the right.

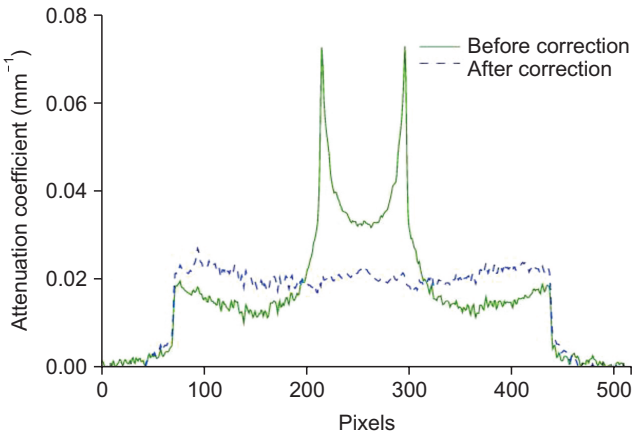

Figure 8. Line profiles of two images along the dashed line shown in Figure 7A. The solid line represents the uncorrected image and dashed line represents the corrected case.

confirmed, the image noise level in the outer ROI is higher than that in the inner ROI. Small square regions were selected from the reconstructed images within the inner and outer ROIs, as shown in Figure 7A and 7B, for a statistical analysis. The absolute noise levels were calculated in the inner and outer ROIs and found to be ±2.3 HU and ±4.1 HU before beam-quality correction and ±2.2 HU and ±4.2 HU after correction, respectively. It is important to note that one can see the spinal structures with much greater visibility in the inner ROI than in the outer ROI, as shown in Figure 7F.

2. Image Registration

Volume images of the pelvis phantom were reconstructed in 512 × 512 × 256 voxels with the same scanning geometry for both the target image and a moving image. The moving image refers to an IWROI image obtained via the proposed scanning method. The moving image was manually rotated ten degrees around the scanning axis and translated (10, 0, 10) pixels with respect to the target image. The moving image was then registered to the target image by maximization of the mutual information. The registration was successfully performed, leading to a translation amount of (10.014, 0.008, 10.084) and rotation of 9.96 degrees. The registration performance is visualized in Figure 9.

3. Dosimetric Measurement

The measured dose using the glass dosimeters is summarized in Table 2. Color-coded dose distributions in the three experiments are shown together with a background film scan in Figure 10A. Shown are no radiation case (top), the proposed method (middle high), the bowtie filter case (middle low), and the case without a filter (bottom). The line profiles along the horizontal line near the bottom edge of the XRCT

https://doi.org/10.4258/hir.2016.22.4.316

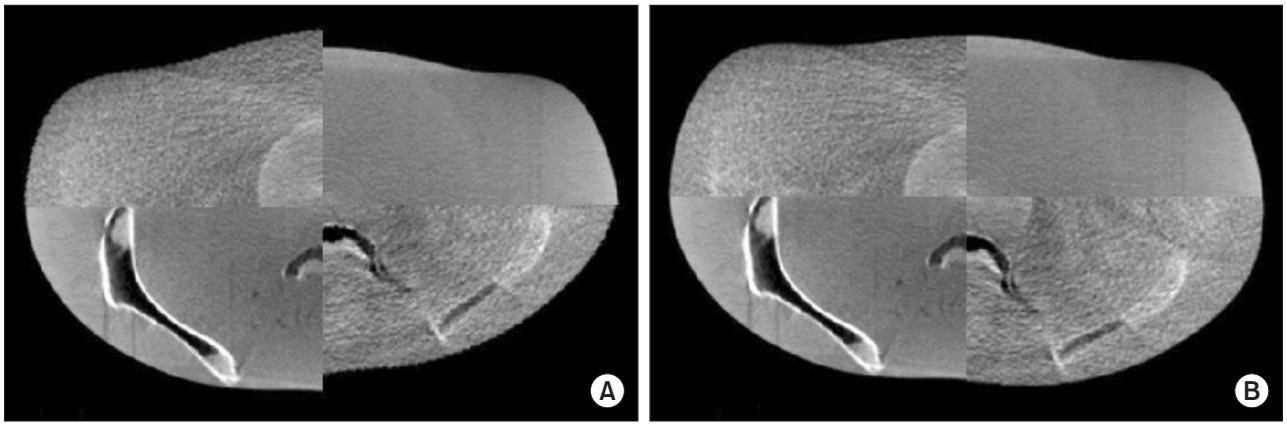

Figure 9. Transverse slice of the target and moving images on a checkerboard: (A) before and (B) after image registration.

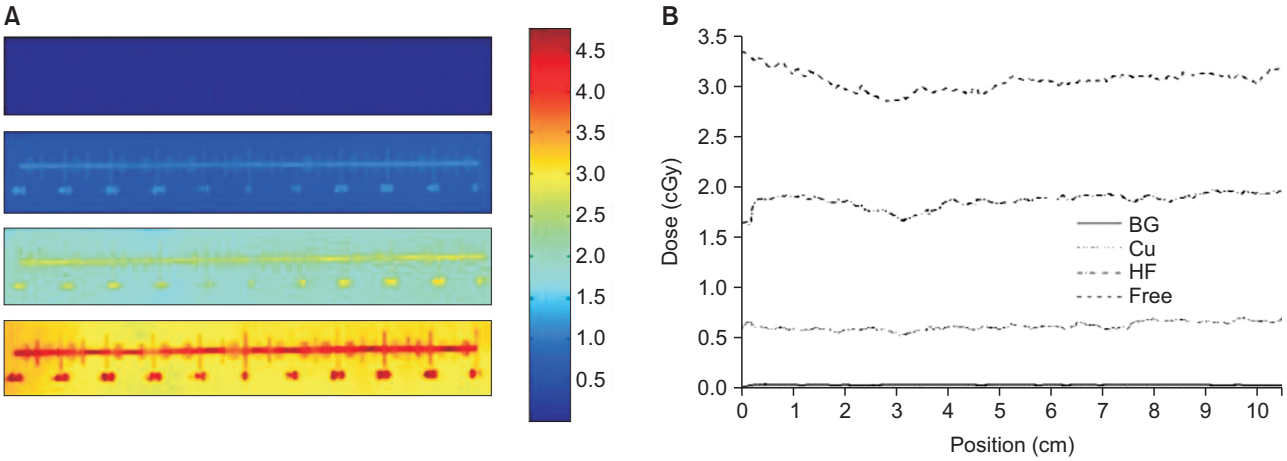

Figure 10. (A) Two-dimensional distribution of the imaging radiation dose (cGy) within the XRCT film for various experiments: no radiation or background (top), proposed method using a Cu filter (middle high), half-fan bowtie filter (middle low), and filter-free case (bottom). (B) Corresponding line profiles along the horizontal line near the bottom edge of the XRCT films are also shown. XRCT: X-ray computed tomography.

Table 2. Dose measurement results

Case	Dose (cGy)		Dose reduction (%)			
			No filter		Bowtie	
	Inner	Outer	Inner	Outer	Inner	Outer
No filter	2.32	3.17	-	-	-	-
Bowtie	1.85	1.78	20.3	43.8	-	-
IW filter	0.72	0.48	69.0	84.9	61.1	73.0

films are also shown in Figure 10B.

IV. Discussion

In this work, we implemented a rebinned BPF algorithm to reconstruct IWROI images from half-fan data acquired by an OBI system. The rebinned BPF algorithm retains the robustness of the BPF against data truncation [15], and it is known to be superior to the original BPF algorithm in terms of numerical stability and computational efficiency [23]. In addition, a considerable advantage when using the BPF algorithm over the FBP is that the BPF algorithm does not need extra off-axis data for image reconstruction in a half-fan mode. Schafer et al. [25] systematically compared various analytic image reconstruction algorithms for half-fan circular CBCT, and their study also demonstrated that the FBP requires redundant data for filtering in general. Strictly speaking, the BPF also needs at least one extra pixel outside the axis projection on the detector to calculate the data derivatives that are to be backprojected onto the chords. However, this is negligibly small compared to the amount of data needed by the FBP for smooth filtering in a half-fan scan.

This advantage can be directly translated to dose management and to enlarging the FOV size in a half-fan CBCT. Particularly, the FOV size, currently limited to 45 cm in the OBI

system due to the off-axis margin, can be increased to 52 cm by shifting the detector almost all of the way toward the rotation axis. This would allow obese patients to be scanned without a loss of information related to data truncation [17]. Although the radiation dose must be carefully assessed with regard to the image quality as an outcome, the proposed half-fan scanning method would at least remove a weighting step to handle redundant data and which often results in suboptimal image quality at a given dose. Throughout the study, we assumed that the imaging target is positioned near the isocenter of the linac system. This is a valid assumption because most radiation therapy systems deliver treatment radiation to a target positioned at the isocenter. If the treatment target is located deep and close to the center of the body, the entire body anatomy would fit in the FOV. Otherwise, it is likely to invoke transverse data truncation, which may affect the image quality adversely. However, the proposed method can provide a more enlarged FOV as compared to a conventional half-fan scan, thereby increasing the likelihood of scanning a patient without data truncation. In addition, the rebinned BPF algorithm can handle data truncation more robustly than FBP algorithms. Therefore, practitioners of IGRT of an off-center target in an obese patient may find the proposed method very useful.

The dose measurement results here clearly indicate the benefits of the proposed method in terms of reducing the imaging radiation dose. However, the dose distribution on the measurement plane may appear counter-intuitive initially; the dose deposited onto the outer ROI is comparable to or even larger than that deposited onto the inner ROI. Considering the scanning geometry of the proposed method, one can conjecture that the inner ROI is subject to a higher exposure level than the outer ROI. This is perhaps attributed to the facts that an exact half-fan scanning geometry was used in this work and that the dose at diagnostic X-ray energies shows a decreasing curve as a function of the depth, leaving the maximum dose close to the entrance surface.

It is important to emphasize the difference between the IW filter used in this work and the half-fan bowtie filter. The primary purpose of using a half-fan bowtie filter is to increase the overall image quality considering the elliptical shape of a typical human torso on the transverse plane. The thicker part of the filter compensates for the thinner or less attenuated parts of the body, resulting in more uniform signal detection throughout the FOV. In contrast, the IW filter is positioned for the purpose of reducing the radiation dose at the cost of sacrificing the image quality in the filtered zone. Although the bowtie filter also contributes to reducing the radiation dose, its dose-saving performance is limited, as is demonstrated here. In addition, the proposed method can be synergistically applied in conjunction with existing techniques of low-dose CT; e.g., one may apply a denoising algorithm such as the penalized weighted least-squares algorithm or bilateral filtering to improve the image noise property if necessary [26,27].

In conclusion, as an attempt to reduce the imaging radiation dose to patients in CBCT for IGRT, we proposed a half-fan-based IWROI imaging technique. A rebinned BPF algorithm was implemented to reconstruct images from half-fan circular cone-beam data. It was shown that the IWROI method substantially reduces the imaging radiation dose and provides reconstructed images with an acceptable level of quality for patient setup and target localization. The proposed half-fan-based IWROI imaging technique can add a valuable option to CBCT in IGRT applications.

Conflict of Interest

No potential conflict of interest relevant to this article was reported.

Acknowledgments

The authors would like to thank Mr. Jung Suk Shin and Mr. Eunhyuk Shin for their help with the EBT2 film calibration at the Samsung Medical Center. This work was supported by grants from the National Research Foundation of Korea (NRF-2013M2A2A9043476 and 2015M3A9E2066998), and by a grant from the Korea Evaluation Institute of Industrial Technology (KEIT) (No. 10051357). It was also supported in part by the KUSTAR-KAIST Institute, Korea, under the R&D program supervised by KAIST.

References

1. Chen GT, Sharp GC, Mori S. A review of image-guided radiotherapy. Radiol Phys Technol 2009;2(1):1-12.
2. Murphy MJ, Balter J, Balter S, BenComo JA Jr, Das IJ, Jiang SB, et al. The management of imaging dose during image-guided radiotherapy: report of the AAPM Task Group 75. Med Phys 2007;34(10):4041-63.
3. Sidky EY, Kao CM, Pan X. Accurate image reconstruction from few-views and limited-angle data in divergent-beam CT. J Xray Sci Technol 2006;14(2):119-39.
4. Sidky EY, Pan X. Image reconstruction in circular cone-beam computed tomography by constrained, total-vari-

 https://doi.org/10.4258/hir.2016.22.4.316

ation minimization. Phys Med Biol 2008;53(17):4777-807.
5. Bian J, Siewerdsen JH, Han X, Sidky EY, Prince JL, Pelizzari CA, et al. Evaluation of sparse-view reconstruction from flat-panel-detector cone-beam CT. Phys Med Biol 2010;55(22):6575-99.
6. Wang J, Li T, Xing L. Iterative image reconstruction for CBCT using edge-preserving prior. Med Phys 2009; 36(1):252-60.
7. Jia X, Lou Y, Li R, Song WY, Jiang SB. GPU-based fast cone beam CT reconstruction from undersampled and noisy projection data via total variation. Med Phys 2010; 37(4):1757-60.
8. Yan H, Cervino L, Jia X, Jiang SB. A comprehensive study on the relationship between the image quality and imaging dose in low-dose cone beam CT. Phys Med Biol 2012;57(7):2063-80.
9. Chityala RN, Hoffmann KR, Bednarek DR, Rudin S. Region of interest (ROI) computed tomography. Proc SPIE Int Soc Opt Eng 2004;5368:534-41.
10. Chen L, Shaw CC, Altunbas MC, Lai CJ, Liu X, Han T, et al. Feasibility of volume-of-interest (VOI) scanning technique in cone beam breast CT: a preliminary study. Med Phys 2008;35(8):3482-90.
11. Cho S, Pearson E, Pelizzari CA, Pan X. Region-of-interest image reconstruction with intensity weighting in circular cone-beam CT for image-guided radiation therapy. Med Phys 2009;36(4):1184-92.
12. Schafer S, Noel PB, Walczak AM, Hoffmann KR. Filtered region of interest cone-beam rotational angiography. Med Phys 2010;37(2):694-703.
13. Kolditz D, Kyriakou Y, Kalender WA. Volume-of-interest (VOI) imaging in C-arm flat-detector CT for high image quality at reduced dose. Med Phys 2010;37(6):2719-30.
14. Zou Y, Pan X, Sidky EY. Image reconstruction in regions-of-interest from truncated projections in a reduced fan-beam scan. Phys Med Biol 2005;50(1):13-27.
15. Cho S, Bian J, Pelizzari CA, Chen CT, He TC, Pan X. Region-of-interest image reconstruction in circular cone-beam microCT. Med Phys 2007;34(12):4923-33.
16. Cho PS, Rudd AD, Johnson RH. Cone-beam CT from width-truncated projections. Comput Med Imaging Graph 1996;20(1):49-57.
17. Ohnesorge B, Flohr T, Schwarz K, Heiken JP, Bae KT. Efficient correction for CT image artifacts caused by objects extending outside the scan field of view. Med Phys 2000;27(1):39-46.
18. Feldkamp LA, Davis LC, Kress JW. Practical cone-beam algorithm. J Opt Soc Am A 1984;1(6):612-9.
19. Yu L, Pelizzari C, Pan X, Riem H, Munro P, Kaissl W. Application of asymmetric cone-beam CT in radiotherapy. Proceedings of 2004 IEEE Nuclear Science Symposium Conference Record; 2004 Oct 16-22; Rome, Italy. p. 3249-52.
20. Leng S, Zhuang T, Nett BE, Chen GH. Exact fan-beam image reconstruction algorithm for truncated projection data acquired from an asymmetric half-size detector. Phys Med Biol 2005;50(8):1805-20.
21. Zou Y, Pan X. Image reconstruction on PI-lines by use of filtered backprojection in helical cone-beam CT. Phys Med Biol 2004;49(12):2717-31.
22. Li L, Chen Z, Zhang L, Xing Y, Kang K. A cone-beam tomography system with a reduced size planar detector: a backprojection-filtration reconstruction algorithm as well as numerical and practical experiments. Appl Radiat Isot 2007;65(9):1041-7.
23. Yu L, Xia D, Zou Y, Sidky EY, Bian J, Pan X. A rebinned backprojection-filtration algorithm for image reconstruction in helical cone-beam CT. Phys Med Biol 2007;52(18):5497-508.
24. Turbell H. Cone-beam reconstruction using filtered backprojection [dissertation]. Linkoping, Sweden: Linkoping University; 2001.
25. Schafer D, Grass M, van de Haar P. FBP and BPF reconstruction methods for circular X-ray tomography with off-center detector. Med Phys 2011;38 Suppl 1:S85.
26. Wang J, Li T, Lu H, Liang Z. Penalized weighted least-squares approach to sinogram noise reduction and image reconstruction for low-dose X-ray computed tomography. IEEE Trans Med Imaging 2006;25(10):1272-83.
27. Wang J, Zhu L, Xing L. Noise reduction in low-dose x-ray fluoroscopy for image-guided radiation therapy. Int J Radiat Oncol Biol Phys 2009;74(2):637-43.